

Long-Range Embedding of Molecular Ions and Excitations in a Polarizable Molecular Environment

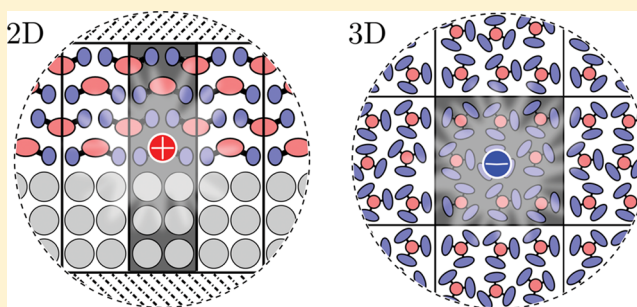
Carl Poelking^{*,†,‡} and Denis Andrienko^{*,†}

[†]Max Planck Institute for Polymer Research, Ackermannweg 10, 55128 Mainz, Germany

[‡]Heidelberg Graduate School of Fundamental Physics, INF 226, 69120 Heidelberg, Germany

S Supporting Information

ABSTRACT: We present a method for evaluating electrostatic and polarization energies of a localized charge, charge transfer state, or exciton embedded in a neutral molecular environment. The approach extends the Ewald summation technique to polarization effects, rigorously accounts for the long-range nature of the charge-quadrupole interactions, and addresses aperiodic embedding of the charged molecular cluster and its polarization cloud in a periodic environment. We illustrate the method by evaluating the density of states and ionization energies in thin films and heterostructures of organic semiconductors. By accounting for long-range mesoscale fields, we obtain the ionization energies in both crystalline and mesoscopically amorphous systems with high accuracy.



1. INTRODUCTION

Knowledge of the energy landscape for charge and energy transport is key to the optimization of organic optoelectronic devices,¹ understanding of photosynthesis in biological systems,² of molecular catalysis³ and chemical sensors.⁴ It is, however, still a challenge in computational materials science to predict these landscapes and to establish their connection to device characteristics.^{5–10} One of the major issues here is the limited system sizes used in today's simulations. They are frequently insufficient to sample the tail of the densities of states^{8,11–13} or long-wavelength spatial correlations of the energy landscape.^{14,15} The need to go beyond a nanometer length scale is also given by the fact that in ordered molecular systems the interaction of a charge with the molecular surrounding is long range. For charge-quadrupole interactions, for instance, the corresponding sum is only conditionally convergent in 3D^{16–20} and converges extraordinarily slowly in 2D systems, such as thin organic films.

In illustration of this, Figure 1a shows the electrostatic contribution to the energies of a neutral molecule, its cation and anion in a molecular crystal of the solar-cell donor compound DSM.²¹ The dependence on the size of the molecular cluster, d_c , reflects the electrostatic energy convergence in 3D- and 2D-periodic systems. Figure 1a may give the false impression that energy levels are converged for a cluster size of 8 nm, when, in fact, the interaction sum is only conditionally converged. It corresponds to spherical shell-by-shell growth of the cluster and will differ for other (cylindrical, cuboidal, etc.) cluster shapes. Figure 1b shows how these energies change in a crystalline thin film. For charges embedded in a 20 nm thin film (Figure 1b), convergence is absolute but is not achieved even for cluster sizes larger than 100 nm. Finally,

in Figure 1c the electrostatic contribution is shown for a charge transfer (CT) state at a donor–acceptor (DSM–C₆₀) interface comprised of two thin films of DSM and the fullerene C₆₀. The electrostatic contribution to the energy of CT states converges faster, whereas the individual contributions of the CT-hole and CT-electron still exhibit the same slow thin film convergence behavior.

As long-range crystalline and liquid-crystalline ordering characterizes many organic materials,^{22,23} an account of long-range effects becomes indispensable in heterogeneous environments, in particular, at interfaces. Such structures are at the heart of many functional devices, e.g., planar heterojunction solar cells, field effect transistors, and organic light-emitting diodes. Typical film thicknesses employed in these devices are on the order of tens of nanometers, whereas surface areas exceed square micrometers. Hence, the molecular arrangement in the out-of-plane dimension can be simulated to scale, whereas the in-plane dimensions have to be modeled effectively through periodic boundary conditions.

Following up on applications to organic interfaces^{16,17} and mixtures,²⁴ in this work, we focus on the technical implementation, further verification, and complementary illustrations of the method designed to evaluate ionization energies (IEs) and electron affinities (EAs) of molecules embedded in such a periodic molecular environment. In what follows, we hence focus on molecular ions embedded in a neutral environment; the method is, however, applicable to any type of embedded molecular excitation, including charge transfer and excited states.

Received: June 13, 2016

Published: July 27, 2016

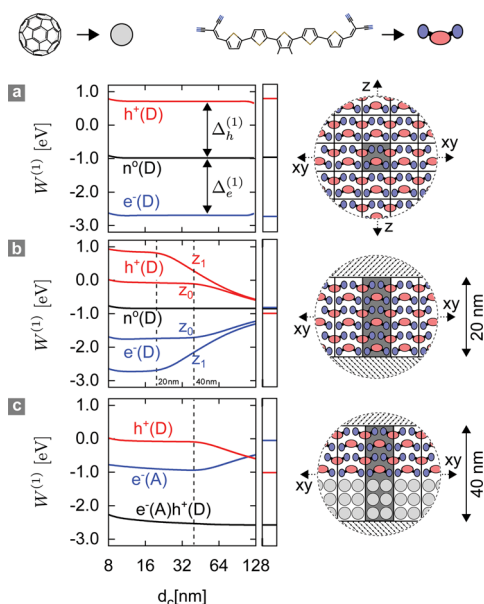


Figure 1. Variation of electrostatic energies $W^{(1)}$ with the cluster size d_c for a bulk (a) and thin film (b,c) setup. Only static atomic multipoles up to quadrupoles are accounted for. In (a) and (b), black, red, and blue lines denote trends for neutral (n^0), hole (h^+), and electron (e^-) states, localized on a donor (D, here: DSM) or acceptor (A, here: C_{60}) molecule, respectively. In (b), z_0 and z_1 refer to a molecular ion positioned at the center and surface of the film, respectively. In (c), the black line denotes the convergence for an interfacial charge transfer state. Energies $W^{(1)}$ for the infinite systems are shown on the very right of each plot, where for the bulk setup a spherical shape factor has been used to remove the conditional convergence, which corresponds to the spherical shell-by-shell growth of the molecular cluster of size d_c . The schematics on the right-hand side indicate the system under study including cartoons of the two molecules, DSM and fullerene, with a repeat unit colored in black, and periodicity indicated by dashed arrows.

Addressing both electrostatic and polarization contributions, the approach adapts and extends the Ewald summation technique^{25,26} in three ways. First, it incorporates induction, which is not originally part of the formalism but can be added.²⁷ Second, it addresses the long-range nature of the charge-quadrupole interaction. Third, it adapts the Ewald method to “broken” periodicities that result when embedding the charged molecular cluster and its polarization cloud in an otherwise periodic system. We illustrate that a long-range treatment is crucial for the description not only of crystalline systems but also of energy correlations and level alignment in mesoscopically amorphous materials.

2. GENERAL FORMALISM

In this section, we outline the implementation of our approach. To make simulations of large, atomistically resolved systems computationally feasible, we use polarizable force fields based on distributed atomic properties.^{28–31} The basics of this concept are recapitulated in the next section. Readers familiar with the perturbative treatment of electrostatic interactions and polarization energies can move directly to Section 2.2.

2.1. Polarization Energy and Work. In weakly interacting molecular assemblies, key corrections to energy levels of molecular ions result from the electrostatic and polarization interaction with the environment. Both interactions lead to energy contributions on the order of 1 eV and can be treated

perturbatively.³² The electrostatic and polarization contributions correspond to the first- and second-order corrections $W_s^{(1)}$ and $W_s^{(2)}$, respectively, where the subscript s denotes the state (hole, electron, neutral) of the molecule. The energy correction Δ_s to IEs ($s = h$) and EAs ($s = e$) due to the environment then reads

$$\Delta_s = \Delta_s^{(1)} + \Delta_s^{(2)} \quad (1)$$

where $\Delta_s^{(i)} = W_s^{(i)} - W_n^{(i)}$; n references the neutral ground state. The IE of a molecule, for example, follows as $IE = IE_0 + \Delta_h$; here, IE_0 denotes the gas-phase ionization energy to be calculated on a quantum-mechanical level. For electron, excitonic or charge-transfer states, analogous expressions hold.

The perturbative correction to the molecular site energy, $W_s = W_s^{(1)} + W_s^{(2)}$, is calculated in a classical expansion of the molecular field and field response in terms of distributed multipoles²⁸ and polarizabilities,³³ respectively, positioned at (typically) atomic expansion sites. Here, W_s then follows from a variational principle, which replaces Poisson’s equation $\nabla(\epsilon \nabla \phi) \sim \rho$ in this microscopic, particle-based picture

$$\frac{\delta W_s}{\delta \Delta Q_{lm}^{a(s)}} = 0 \quad (2)$$

Its self-consistent solution consists of the set of multipolar (here, dipolar) moments $\Delta Q_{lm}^{a(s)}$ induced at the (atomic) expansion sites, a , with local polarizabilities α_{lm}^a in response to the permanent multipolar moments $Q_{lm}^{a(s)}$ that approximate the molecular, unperturbed charge densities. The set $\{\Delta Q_{lm}^{a(s)}\}$ constitutes the polarization state of the system and, together with $\{Q_{lm}^{a(s)}\}$, determines $W_s^{(1)}$ and $W_s^{(2)}$, and finally Δ_s . We note that $W_s^{(2)}$, different from $\Delta_s^{(2)}$, only takes negative values, as is characteristic of a second-order perturbative term.

The self-interaction energy W_s of the molecular system is normally decomposed into external and internal contributions, the latter reflecting the positive polarization work³²

$$W_s = W_{\text{ext}}[\mathcal{D}^{(s)}; \mathcal{D}^{(s)}] + W_{\text{int}}[\mathcal{D}^{(s)}] \quad (3)$$

$$W_{\text{ext}}[\mathcal{D}^{(s)}; \mathcal{D}^{(s)}] = \frac{1}{2} \sum_{M^{(s)}} \sum_{M'^{(s)} \neq M^{(s)}} (Q_t^{a(s)} + \Delta Q_t^{a(s)}) T_{tu}^{aa'} (Q_u^{a'(s)} + \Delta Q_u^{a'(s)}) \quad (4)$$

$$W_{\text{int}}[\mathcal{D}^{(s)}] = \frac{1}{2} \sum_M \Delta Q_t^{a(s)} (\alpha^{-1})_{tu}^{ab(s)} \Delta Q_u^{b(s)} \quad (5)$$

Here, $\mathcal{D}^{(s)}$ is a discrete, multipolar charge density—it denotes the entire set of static and induced multipoles in the system. The notation $W_{\text{ext}}[\mathcal{D}^{(s)}; \mathcal{D}^{(s)}]$ emphasizes that the summation is performed over all pairs of molecules.

Following Stone’s notation,³² Q_t^a and $Q_u^{a'}$ are multipole moments in a spherical-tensor representation, with angular and magnetic quantum numbers contracted into a single index. Here, $T_{tu}^{aa'}$ are tensors that mediate the interaction between multipole moments Q_t^a and $Q_u^{a'}$ of atoms a and a' .³⁴ For both atomic indices ($a, b \in M$ and $a' \in M'$) as well as tensorial components (t and u), Einstein sum conventions are in place.

For computational efficiency, we truncate the expansion of the molecular charge density (distributed multipole analysis²⁸) after rank $l = 2$, such that atomic quadrupoles are still accounted for. Also, we employ distributed polarizabilities in a

local-dipole approximation ($\alpha_{tu}^{ab} \rightarrow \alpha_t^a \neq 0$ if $t \in \{1x, 1y, 1z\}$) as developed by Thole,^{30,35} hence disregarding charge-flow effects.²⁹ In organic solids with their spatially rapidly fluctuating fields, charge flow is expected to play only a minor role. A local-dipole scheme is therefore sufficient to capture polarization effects. In order to avoid an unphysical overpolarization to which atomic-dipole schemes are susceptible,³⁰ the Thole model requires damping of induced–induced interactions at short separations. The interaction tensors $T_{tu}^{aa'}$ in eq 4 are hence modified such that terms with a distance scaling of $R^{-\nu}$ are multiplied by a damping function $\Lambda_{2\nu+1}$ listed in Section S3 of the Supporting Information. Furthermore, due to the larger polarizabilities of *conjugated* molecules in comparison to biological compounds, the set of Thole polarizabilities³⁵ is scaled iteratively in order to match the volume of the polarizability ellipsoid ($\sim 1/\prod_{i=1}^3 \sqrt{\tilde{\alpha}_i}$, where $\tilde{\alpha}_i$ is the i -th eigenvalue of the molecular polarizability tensor) calculated here using density functional theory.

2.2. Aperiodic–Periodic Decomposition. In the following, we detail how eq 2 is solved for an *aperiodic* (i.e., not periodically repeated) charged molecule embedded in a *periodic*, neutral, polarizable environment, and how the associated perturbative contributions $\Delta_s^{(1)}$ and $\Delta_s^{(2)}$ are evaluated with an infinite interaction range applied to all particles.

Since a fully self-consistent solution of eq 2 for the entire system (incorporating all periodic images as well as a single charged molecule) is difficult to achieve even in principle, we first introduce a cutoff for the polarization of the environment by the excess charge. This cutoff controls up to where the introduction of this charge modifies the polarization state of the environment. The assumption of such a finite “polarization cloud” is readily justified: The charge-induced dipole interaction energy has a $1/r^4$ decay and is hence absolutely convergent. The polarization cloud then has to be chosen only large enough to prevent discontinuities in the fields across its boundary.

To deal with the broken periodicity, we spatially partition the multipolar charge density $\mathcal{D}^{(s)}$ onto several subsets. Once again, the superscript s denotes the state of the embedded molecule; e.g., $s = n$ would correspond to the neutral state. Now, let us denote by \mathcal{B} the set of molecules in the simulation box, with all molecules in their *neutral* charge configuration. The entire ground-state system \mathcal{B}^* then consists of \mathcal{B} and its periodic replicas. Charging of the embedded molecule, $X^{(s)}$, modifies this charge density by polarizing the surrounding molecules. We correspondingly denote the set of molecules in the polarization cloud by $\mathcal{P}^{(s)}$. We will refer to the rest of the system, $\tilde{\mathcal{B}}^* = \mathcal{B}^* \setminus \mathcal{P}^{(s)}$, as the background. The system partitioning is illustrated in Figure 2.

On the basis of eq 3, the energy correction W_s then reads

$$W_s = W_{\text{ext}}[\mathcal{P}^{(s)}; \mathcal{P}^{(s)}] + W_{\text{ext}}[\mathcal{P}^{(s)}; \tilde{\mathcal{B}}^*] + W_{\text{ext}}[\tilde{\mathcal{B}}^*; \tilde{\mathcal{B}}^*] + W_{\text{int}}[\mathcal{P}^{(s)}] + W_{\text{int}}[\tilde{\mathcal{B}}^*] \quad (6)$$

Here, W_{ext} denotes the intermolecular field interaction energy and W_{int} the intramolecular induction work, as defined in eqs 4 and 5. The polarization cloud (Figure 2c) is chosen large enough to screen the excitation from $\tilde{\mathcal{B}}^*$, whose polarization state is thus assumed unaffected. Therefore, no state index s is used for the contributions $W_{\text{ext}}[\tilde{\mathcal{B}}^*; \tilde{\mathcal{B}}^*]$ and $W_{\text{int}}[\tilde{\mathcal{B}}^*]$, which

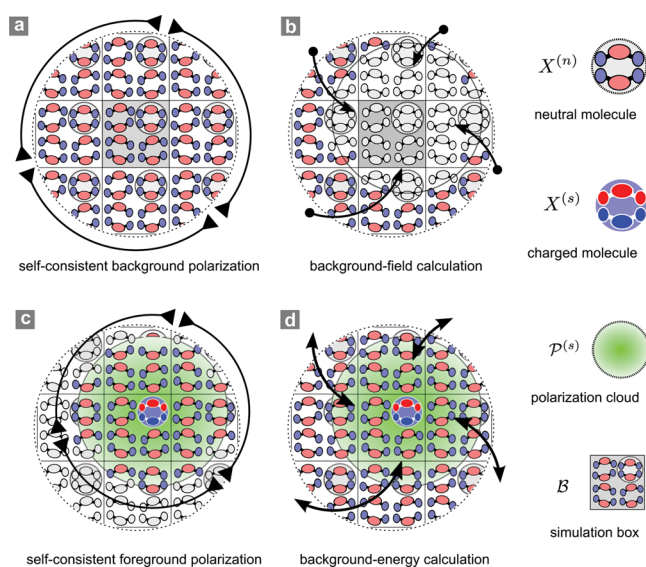


Figure 2. Computational workflow. (a) Computation of the polarization state of the periodic ground-state system. The simulation box \mathcal{B} , colored in gray, incorporates the molecular cluster in its neutral ground state, $X^{(n)}$. (b) Calculation of background fields acting on the polarization cloud (foreground) $\mathcal{P}^{(s)}$ centered around the charged cluster $X^{(s)}$. (c) Self-consistent polarization within $\mathcal{P}^{(s)}$ and evaluation of the self-energy of $\mathcal{P}^{(s)}$. (d) Evaluation of the interaction energy between the foreground $\mathcal{P}^{(s)}$ and the polarized background $\tilde{\mathcal{B}}^*$.

will in fact cancel when taking the difference $\Delta_s^{(i)} \equiv W_s^{(i)} - W_n^{(i)}$ and hence need not be calculated. The surviving terms from eq 6 read as follows:

$$W_{\text{ext}}[\mathcal{P}^{(s)}; \mathcal{P}^{(s)}] = \frac{1}{2} \sum_P \sum_{P' \neq P} \left(Q_t^{p(s)} + \Delta Q_t^{p(s)} \right) T_{tu}^{pp'} \left(Q_u^{p'(s)} + \Delta Q_u^{p'(s)} \right) \quad (7)$$

$$W_{\text{ext}}[\mathcal{P}^{(s)}; \tilde{\mathcal{B}}^*] = \sum_P \sum_{\tilde{\mathcal{B}}^*} \left(Q_t^{p(s)} + \Delta Q_t^{p(s)} \right) T_{tu}^{pp} \left(Q_u^{b(n)} + \Delta Q_u^{b(n)} \right) \quad (8)$$

$$W_{\text{int}}[\mathcal{P}^{(s)}] = \frac{1}{2} \sum_P \Delta Q_t^{p(s)} (\alpha^{-1})_t^{a(s)} \Delta Q_t^{p(s)} \quad (9)$$

Here, $p(s)$ denotes an atom of a molecule $P^{(s)}$ in a polarization cloud $\mathcal{P}^{(s)}$, where s is the state of the molecule (neutral, anion, cation) and b enumerates atoms in the polarized background $\tilde{\mathcal{B}}^*$. In these expressions, induced moments have to be calculated self-consistently on the basis of eq 2, yielding the linear system of equations^{27,32}

$$\Delta Q_t^{p(s)} = - \sum_{\tilde{\mathcal{B}}^*} \alpha_t^{p(s)} T_{tu}^{pb} \left(Q_u^{b(n)} + \Delta Q_u^{b(n)} \right) - \sum_P \alpha_t^{p(s)} T_{tu}^{pp'} \Delta Q_u^{p'(s)} \quad (10)$$

Note that in eqs 7 and 9, $W_{\text{ext}}[\mathcal{P}^{(s)}; \mathcal{P}^{(s)}]$ and $W_{\text{int}}[\mathcal{P}^{(s)}]$ only count interactions within $\mathcal{P}^{(s)}$: Direct evaluation is therefore possible at reasonable computational expense. Here, $W_{\text{ext}}[\mathcal{P}^{(s)}; \tilde{\mathcal{B}}^*]$ (eq 8), by contrast, comprises the interaction

of $\mathcal{P}^{(s)}$ with the infinite but *semiperiodic* set $\tilde{\mathcal{B}}^*$. In order to use the Ewald summation technique, designed for periodic systems, we add the foreground density $\mathcal{P}^{(n)}$ in its neutral charge and polarization state to $\tilde{\mathcal{B}}^*$, thus allowing for the transformation into reciprocal space, and subsequently correct for this addition in real space. Higher-order fields and interaction tensors follow by taking spatial derivatives with regard to the coordinates of the source and target atomic positions.

$W_{\text{ext}}[\mathcal{P}^{(s)}; \tilde{\mathcal{B}}^*]$ is then obtained as the sum over five contributions (the derivation is sketched in Sections S8 and S9 of the Supporting Information),

$$\begin{aligned} W_{\text{ext}}[\mathcal{P}^{(s)}; \tilde{\mathcal{B}}^*] &= W_k[\mathcal{P}^{(s)}; \mathcal{B}] + W_r[\mathcal{P}^{(s)}; \tilde{\mathcal{B}}^*] \\ &\quad - W_{\text{sil}}[\mathcal{P}^{(s)}; \mathcal{P}^{(n)}] - W_c[\mathcal{P}^{(s)}; \mathcal{P}^{(n)}] \\ &\quad + W_*[\mathcal{P}^{(s)}; \mathcal{B}] \end{aligned} \quad (11)$$

The first four terms on the right-hand side are

$$W_k[\mathcal{P}^{(s)}; \mathcal{B}] = \frac{1}{4\pi\epsilon_0} \frac{4\pi}{V} \sum_{\vec{k} \neq 0} S(\vec{k}; [\mathcal{P}^{(s)}]) S^*(\vec{k}; [\mathcal{B}]) A(k) \quad (12)$$

$$W_r[\mathcal{P}^{(s)}; \tilde{\mathcal{B}}^*] = \frac{1}{4\pi\epsilon_0} \sum_{\tilde{\mathcal{B}}^*} \sum_{\mathcal{P}^{(s)}} \sum_{\nu=0}^4 T_\nu^{pb} \Lambda_{2\nu+1}^{pb} B_\nu(R_L^{pb}) \quad (13)$$

$$\begin{aligned} W_{\text{sil}}[\mathcal{P}^{(s)}; \mathcal{P}^{(n)}] &= \frac{1}{4\pi\epsilon_0} \sum_{\mathcal{P}} \left(\frac{2\beta}{\sqrt{\pi}} q^{p(s)} q^{p(n)} + \frac{4\beta^3}{3\sqrt{\pi}} \bar{\mu}^{p(s)} \right. \\ &\quad \left. \bar{\mu}^{p(n)} + \frac{16\beta^5}{5\sqrt{\pi}} \bar{\theta}^{p(s)} : \bar{\theta}^{p(n)} \right) \end{aligned} \quad (14)$$

$$W_c[\mathcal{P}^{(s)}; \mathcal{P}^{(n)}] = \frac{1}{4\pi\epsilon_0} \sum_{p(s)} \sum_{p(n) \neq p(s)} \sum_{\nu=0}^4 T_\nu^{pp'} C_\nu(R_0^{pp'}) \quad (15)$$

The first three contributions in eq 11 (eqs 12–14) are the standard Ewald terms for the reciprocal- and real-space interaction and self-interaction correction, respectively. Their interaction kernels take into account higher-order permanent and induced moments^{36,37} and, in the case of $W_r[\mathcal{P}^{(s)}; \tilde{\mathcal{B}}^*]$, incorporate short-range damping functions $\Lambda_{2\nu+1}$ as discussed above.

For the real- and reciprocal-space terms, the anisotropic interaction kernels S and T_ν (the former is the structure factor of the multipolar density) capture the orientation dependence of the interaction between two sets of atomic multipoles in the respective space; they are listed in Section S1 of the Supporting Information. The associated isotropic interaction kernels $A(k)$ and $B_\nu(R)$ (Section S2, Supporting Information) yield the distance dependence. Finally, the real-space interaction is damped by the damping function $\Lambda_{2\nu+1}$ prescribed by $B_\nu(R)$, which scales as $R^{-(2\nu+1)}$ for sufficiently small distances (see Section S3, Supporting Information, for details). In the above equations, the set of atom-centered multipoles incorporates the atomic charge q , dipole $\bar{\mu}$, and quadrupole $\bar{\theta}$, now in their Cartesian representation. Note that the quadrupole is here defined as $\theta_{\alpha\beta} = \sum_a q^a \left[\frac{1}{2} r_a^\alpha r_a^\beta - \frac{1}{6} \delta_{\alpha\beta} (r^a)^2 \right]$, which differs from the conventional definition by a factor $\frac{1}{3}$. Also note that the sum $\sum_{\tilde{\mathcal{B}}^*}$ is in practice implemented as a double sum over

image-box vectors \vec{L} and the periodic density \mathcal{B}^* , with molecules participating in the polarization cloud $\mathcal{P}^{(s)}$ and $\mathcal{P}^{(n)}$ being excluded.

The fourth term in eq 11, $W_c[\mathcal{P}^{(s)}; \mathcal{P}^{(n)}]$, denotes an aperiodic subtraction which corrects for the overlap between $\mathcal{P}^{(s)}$ and $\mathcal{P}^{(n)}$ (see Section S9, Supporting Information, for details). Here, the anisotropic kernel is identical to T_ν from eq 13. The isotropic kernel C_ν , however, differs from B_ν (Section S2, Supporting Information) in that it involves derivatives of the long-ranged $\text{erf}(\beta r)/r$ rather than the short-ranged $\text{erfc}(\beta r)/r$ part of the interaction. The $\mathcal{P}^{(n)} = \mathcal{P}^{(s)}$ terms have already been accounted for in the self-interaction term, eq 14.

The fifth term in eq 11, $W_*[\mathcal{P}^{(s)}; \mathcal{B}]$, is a shape ($k = 0$) contribution that tackles the conditionality of the interaction sum. An analogous conditionality arises in overall neutral systems with a net dipole moment of the periodically repeated charge density \mathcal{B} ,²⁰ as is often encountered in molecular systems. As a result, the convergence of the interaction sum depends on the (macroscopic) summation shape. Here, we treat molecular solids, where a second conditionality arises from the net charge that resides in $\mathcal{P}^{(s)}$ and interacts with a net-quadrupolar background. Shape terms for the case of a macroscopic cube and slab summation shape are derived as (see Section S8, Supporting Information, for details)

$$\begin{aligned} W_*^{\text{cube}}[\mathcal{P}^{(s)}; \mathcal{B}] &= -\frac{1}{4\pi\epsilon_0} \frac{4\pi}{3V} \left(Q_0^{\mathcal{P}^{(s)}} \text{Tr}[\tilde{\Theta}^{\mathcal{B}^{(n)}}] \right. \\ &\quad \left. + Q_0^{\mathcal{B}^{(n)}} \text{Tr}[\tilde{\Theta}^{\mathcal{P}^{(s)}}] - \vec{M}^{\mathcal{P}^{(s)}} \cdot \vec{M}^{\mathcal{B}^{(n)}} \right) \end{aligned} \quad (16)$$

$$\begin{aligned} W_*^{\text{slab}}[\mathcal{P}^{(s)}; \mathcal{B}] &= -\frac{1}{4\pi\epsilon_0} \frac{4\pi}{V} \left(Q_0^{\mathcal{P}^{(s)}} \Theta_{zz}^{\mathcal{B}^{(n)}} + Q_0^{\mathcal{B}^{(n)}} \Theta_{zz}^{\mathcal{P}^{(s)}} \right. \\ &\quad \left. - M_z^{\mathcal{P}^{(s)}} M_z^{\mathcal{B}^{(n)}} \right) \end{aligned} \quad (17)$$

where eq 16 implies summation over cubic/spherical and eq 17 over infinitely thin slab-shaped shells. The net multipolar moments of the densities $\mathcal{P}^{(s)}$ and \mathcal{B} that feature in these expressions are defined as

$$Q_0^{\mathcal{P}^{(s)}} = \sum_p q^{p(s)} \quad (18)$$

$$\vec{M}^{\mathcal{P}^{(s)}} = \sum_p \left(q^{p(s)} \vec{r}_p + \bar{\mu}^{p(s)} \right)$$

$$\tilde{\Theta}^{\mathcal{P}^{(s)}} = \sum_p \left(\frac{1}{2} q^{p(s)} \vec{r}_p \otimes \vec{r}_p + \bar{\mu}^{p(s)} \otimes \vec{r}_p + \bar{\theta}^{p(s)} \right) \quad (19)$$

Analogous expressions are used for $Q_0^{\mathcal{B}}$, $\vec{M}^{\mathcal{B}}$, and $\tilde{\Theta}^{\mathcal{B}}$.

Equation 11 is the key result of the method: With the cube/sphere shape correction, eq 16, it gives energies of charged clusters in a 3D-periodic lattice with all three periodic directions treated identically in the summation. In order to mimic a 2D-infinite slab (e.g., for calculating IE and EA of thin films), the slab shape correction, eq 17, is used.

2.3. Computational Procedure. Combining our results for energy, field, and polarization calculations, Figure 2 summarizes the procedure to solve eq 2 and compute W_s for a molecular system in a state s . First (Figure 2a), the

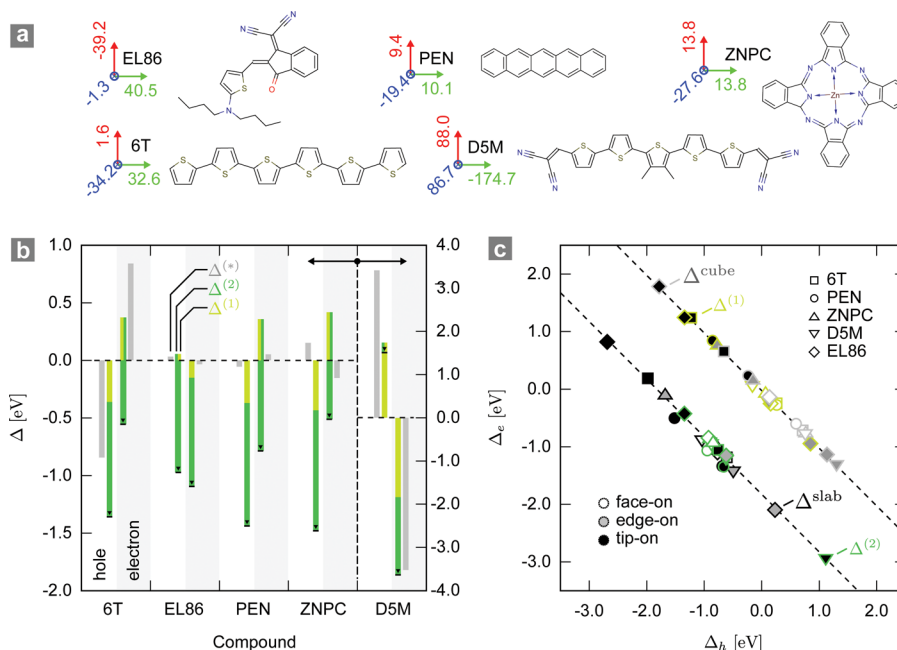


Figure 3. (a) Chemical structures of pentacene (PEN), sexithiophene (6T), zinc phthalocyanine (ZNPC), merocyanine dye EL86,⁴³ and acceptor-substituted oligothiophene DSM,²¹ shown together with the eigenframe of the quadrupole tensor (principal components are indicated in atomic units). (b) Electrostatic ($\Delta^{(1)}$, light green), polarization ($\Delta^{(2)}$, dark green), and cube shape (Δ^{cube} , gray) contributions to electron and hole levels computed from experimental unit cells. The small black bars indicate the total solid-state contribution, Δ^{cube} . Note the different energy scale for DSM. (c) Correlation of electrostatic ($\Delta^{(1)}$) and polarization ($\Delta^{(2)}$) contributions to electron (Δ_e) and hole (Δ_h) site energies for thin film levels calculated for differently oriented unit cells under application of the respective shape contribution. The symbol shape indicates the material (6T, ..., EL86), fill style the configuration (face-on, edge-on, tip-on).

polarization state of the neutral system is computed according to eq 10 and eq S17 (field expression) in the Supporting Information. This step usually needs to be carried out only once for each coordinate configuration. Second (Figure 2b), fields generated by the semiperiodic background across the polarization cloud are calculated, taking into account both permanent and induced moments. Third (Figure 2c), the polarization cloud is polarized self-consistently in the fields of the semiperiodic background. Fourth (Figure 2d), the interaction energy between the semiperiodic background and the polarization cloud, as well as within the polarization cloud, are evaluated using eqs 7, 9, and 11.

The computational cost of the above procedure is mostly due to the self-consistent evaluation of induced dipoles of the polarization cloud (step 3). The cost of this step scales as r_{pc}^6 with the radius r_{pc} of the cloud. Typically, $r_{pc} = 4$ nm proves to be sufficient to converge level profiles, except for a homogeneous dielectric stabilization of the material beyond r_{pc} .

Finally, the long-range stabilization is recovered in an *ad hoc* fashion:³⁸ To this end, we consider the polarization energy of a charge localized in a nonpolarizable spherical cavity with radius r_{pc} embedded in a dielectric of dielectric constant ϵ_1 in the half-space $z > 0$, in the vicinity of an interface with a second dielectric layer of dielectric constant ϵ_2 in $z < 0$ (as frequently encountered in organic electronic devices)

$$\Delta_s^{(\epsilon)}(z > r_{pc}) = -\frac{1}{8\pi\epsilon_0} \frac{q^2}{r_{pc}} \frac{\epsilon_1 - 1}{\epsilon_1} \left[1 + \frac{r_{pc}}{2z} \frac{\epsilon_2 - \epsilon_1}{(\epsilon_1 - 1)(\epsilon_1 + \epsilon_2)} \right] \quad (20)$$

This expression holds for excitations with a net-charge q as leading moment. Higher order moments, as they would apply to net-neutral excitations, in particular, charge transfer states, could be readily treated on the same grounds.³⁸ In practice, the contribution from higher-order moments is, however, negligible—different from charges, where, e.g., $\Delta^{(\epsilon)}$ evaluates to -0.11 eV for a hole or electron embedded in an environment of $\epsilon_1 = \epsilon_2 = 3$ and $r_{pc} = 4$ nm.

3. VALIDATION AND APPLICATIONS

In this section, we first validate electrostatic energies obtained with our method against the existing 2D-Ewald approach by initially excluding all polarization contributions. We then briefly discuss published applications of the method, with benchmarks based on experimentally measured quantities: IEs of thin crystalline films,¹⁶ energies of charge transfer states at donor–acceptor interfaces,¹⁷ and density of states of mixtures of molecular crystals.²⁴ Finally, we apply our method to amorphous mesophases, as encountered in organic solar cells or light-emitting diodes, and show that residual ordering in a small simulation box combined with the cutoff-based approaches can lead to false predictions of molecular energies in amorphous thin films.

3.1. 2D Ewald vs 3D Ewald with Slab Shape Term. For the case of a molecular film sandwiched between two vacuum layers, periodically repeated in all three dimensions, the thin-film shape correction is inversely proportional to the volume of the simulation cell. Hence, by increasing its out-of-plane dimension, while keeping the slab thickness fixed, one can eventually recover the exact result for a 2D-periodic system even without applying a shape term,^{39,40} at the cost, however, of a significantly denser k -vector spacing in reciprocal space. Another option is to use a 2D-Ewald sum^{41,42} with the

underlying formulas listed in Section S6 of the [Supporting Information](#). The comparison of the 2D-Ewald versus 3D-Ewald description (the latter incorporating the slab shape term) is presented in Section S7 of the [Supporting Information](#). The comparison serves as a validation of the approach, at least for neutral nonpolarizable systems with partial charges (the 2D-Ewald formalism has so far been formulated only for electrostatic sums with partial charges, thus excluding atomic polarizabilities and higher-rank multipoles).

The proposed 3D-periodic description has, however, several benefits as compared to the 2D-Ewald method. First, it is more efficient since the reciprocal-space sum conveniently factorizes with respect to the two multipolar densities $\mathcal{P}^{(s)}$ and \mathcal{B} . Second, it is more flexible: It enables the simulation of both thin-film and bulk conditions within the same framework and, on the implementation side, is already capable of treating higher-rank multipoles and polarization effects.

3.2. Ionization Energies of Crystalline Films. The proposed technique is ideally suited for the evaluation of ionization energies (IEs) of thin organic films, routinely performed experimentally using ultraviolet photoelectron spectroscopy (UPS). To benchmark the accuracy of the method, the ionization energies of five different materials ([Figure 3a](#)) in face-on, edge-on and tip-on orientations in thin films were calculated as described by Poelking et al.¹⁶ by adding the thin-film shape contribution to the energy of the periodic 3D system. The resulting IEs agree remarkably well with the experimentally measured energy levels.¹⁶ In fact, the accuracy of the proposed method allows us to deduce molecular orientation from a single IE measurement.

To illustrate the importance of different contributions to the ionization energy, [Figure 3b](#) shows the electrostatic and polarization contributions $\Delta^{(1)}$ and $\Delta^{(2)}$ for both electrons and holes, as well as the shape contribution Δ^{cube} computed from [eq 16](#). Note that the latter includes contributions from both electrostatics and polarization. First, it can be seen that the first-order correction $\Delta^{(1)}$ varies significantly among compounds, as does Δ^{cube} . Here, $\Delta^{(2)}$ is reasonably constant across different materials, ranging between -0.9 and -1.0 eV.

[Figure 3b](#) seems to indicate that there are specific packing modes and molecular layouts, which together energetically favor either holes or electrons. In fact, apart from Δ^{cube} , these exact same results could have also been extracted from a cutoff-based description, which, as seen in [Figure 1a](#), tends to correspond to the cubic/spherical limit implied by [eq 16](#). Such an approach has been used in the past and indeed led to the conclusion that some packing modes (e.g., herringbone vs brickwork) will lead to lower bulk hole energies than others.⁶

A bulk description is, however, not appropriate when simulating devices. Instead, a thin-film description is needed, where IEs depend also on molecular orientation. For illustration, [Figure 3c](#) correlates electron and hole contributions $\Delta^{(1)}$, $\Delta^{(2)}$, and Δ^{cube} , as well as the solid-state contribution Δ^{slab} obtained from the same unit cells as simulated in [Figure 3b](#) but with a slab shape term ([eq 17](#)) applied along the three unit-cell vectors. This procedure mimics different orientations (face-on, edge-on, tip-on) in a thin film, indicated by the fill style of the symbols, next to the symbol shape, which distinguishes between the five compounds. As becomes clear from a comparison of $\Delta^{(1)}$ (light green symbols), general conclusions that link packing modes to electrostatic and polarization contributions are now impossible to formulate without at the same time

accounting for molecular orientation. Specifically, orientations with $Q_{20} > 0$ tend to produce a larger electrostatic stabilization of holes, as predicted by [eq 17](#): For DSM, $Q_{20} > 0$ is associated with a face-on, for PEN, 6T and ZNPC with a tip-on orientation. Generally, the effect of orientation is sufficiently strong to produce both negative and positive $\Delta^{(1)}$'s for the same carrier type.

3.3. Charge Transfer States at Donor–Acceptor Interfaces. Another practical application of our embedding approach is the evaluation of energies of charge transfer (CT) states at the donor–acceptor (DA) interfaces of organic solar cells.¹⁷ Here, the long-range charge quadrupole interactions result in an additional contribution, which either stabilizes or destabilizes the charge transfer state, depending on the orientation and ordering of molecular quadrupoles at the DA interface. In fact, this additional electrostatic potential can lead to a practically barrierless splitting of charge transfer states, which otherwise are strongly bound by the Coulomb attraction. Understanding the link between the photovoltaic gap and charge splitting and detrapping is of course crucial for the design of efficient photovoltaic cells.¹⁷

3.4. Density of States in Mixtures. The proposed method is also suitable for evaluating the density of states of organic semiconductors. In particular, one can show that the long-range electrostatic effects can be exploited to tune the density of states of an organic semiconductor *continuously*, despite the fact that charges are spatially localized.²⁴ Such “bandstructure engineering”, as confirmed by UPS spectroscopy, opens up new opportunities for the design of organic solar cells: The open-circuit voltage of organic solar cells can be continuously tuned by blending different absorber materials.²⁴

3.5. Amorphous Systems. In this section, we consider amorphous semiconductors used in organic light-emitting diodes, where disordered materials are preferred due to their processability and fine miscibility in host–guest systems. Studying amorphous semiconductors in the context of long-range interactions may appear paradoxical since we have already identified ([eqs 16 and 17](#)) that uncompensated multipolar moments are responsible for linking the energetics of microscopic states to mesoscopic order. In amorphous semiconductors, however, these moments should by definition tend to zero on large scales. Still, the question remains on what scale multipolar moments start to decay to give way to an electrostatically isotropic continuum and how this reflects in the energy landscape of these materials.

The atomistic configurations of 4096 molecules of Alq₃¹⁰ were prepared via molecular dynamics simulations with tailored force fields adapted from OPLS-AA.⁴⁶ The starting configurations were first randomized at high temperatures and then quenched to 300 K, with subsequent equilibration over a time period of several nanoseconds. The computed DOS, that is the histogram of solid-state IEs and EAs of all molecules, is shown in [Figure 4a](#). For both IEs and EAs, we employed three different computational procedures: a cutoff-based description (dashed blue lines) and the long-range embedding protocol from [Section 2](#) with either a cubic shape term (dotted-dashed red lines) or no shape term at all (solid black lines). The latter should be thought of as an isotropic limit, which assumes all multipolar moments to average out on a mesoscopic scale.

First, we note that the cutoff-based description and long-range description in the cubic limit match closely. This is not surprising in that both frameworks are virtually identical with respect to their long-range behavior. In particular, a spherical

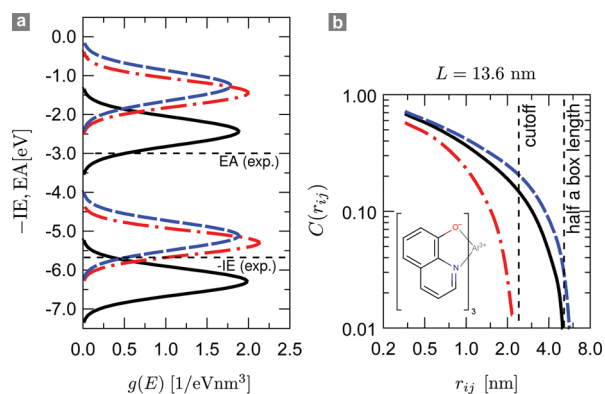


Figure 4. (a) Densities of ionization energies and electron affinities in Alq₃ computed with a cutoff (red dashed-dotted line) and with long-range embedding in the cubic (blue dashed line) or isotropic limit (black solid line). The latter yields much better agreement with ionization energies and electron affinities extracted from photoelectron spectroscopy^{44,45} (horizontal dashed lines). Note that photoelectron spectroscopy probes the tail of the densities of states. (b) Spatial correlation function evaluated with the computational procedure indicated by the line style as described in (a). In the cutoff description, correlations are truncated at the cutoff and in the case of long-range embedding at half the box length, indicative of a finite-size effect.

cutoff always implicitly includes long-range contributions tackled by the shape term in eq 16, as also illustrated by the convergence scan from Figure 1b. The agreement between these two approaches therefore serves as a mere consistency check. More striking is, however, the 1 eV difference between the DOS obtained in the cubic vs isotropic limit, proving that this system, though structurally amorphous, features a conditionality in the interaction sum which is picked up by both the cutoff and cubic limit. This observation implies a challenge for simulations, as it is at this stage impossible to pinpoint the origin of the mesoscopic moments, as they can be due to subtle preferential ordering present also in the real system, or to finite-size-induced fluctuations, or both. If, for example, preferential ordering really plays a role, then how large do system sizes have to be in order to not truncate structural correlations before convergence (at least in a thin-film sense) is achieved? On the other hand, if finite-size effects are exclusively responsible for the observed differences, then the isotropic limit should be a more appropriate description. Indeed, this limit appears to agree better with energy levels extracted experimentally from the DOS onset,^{44,45} as indicated by the dashed horizontal lines in Figure 4a.

In addition to level positioning and alignment, we furthermore consider the spatial correlation function $C(R)$ of the energy landscape, Figure 4b. Correlations of this landscape have been shown to result in the characteristic Poole-Frenkel behavior of the mobility in many organic semiconductors. Figure 4b, however, illustrates that atomistic simulations tend to truncate this correlation function in a cutoff-based description for pair separations larger than the cutoff r_c (here, 3 nm). Even in a long-range description, the finite system size forces correlations to zero at approximately half the box length, with the cubic limit resulting in stronger correlations. In amorphous semiconductors, calculating the DOS and spatial correlations thereof may hence be more involved than initially anticipated: In particular, large system sizes (to be tackled with advanced simulation protocols) will be required in order to disentangle finite-size artifacts from ordering effects. This

challenge has a direct link to compound screening for organic light emitting diodes, where tuning of level alignment is crucial in order to guarantee device functionality and bypass degradation mechanisms.⁴⁷

4. CONCLUSIONS

The long-range polarized embedding approach presented in this work targets the quantitative evaluation of the energy landscape of charge carriers, charge transfer, and excited states in molecular systems. Implemented in the VOTCA package,¹⁰ it can be readily parametrized from first principles, while accounting for both polarization and electrostatic effects. In particular, it successfully copes with the slowly convergent charge-quadrupole interaction encountered in many molecular materials.

Using this approach, we illustrated the effect of molecular orientation and order on energy level profiles in thin crystalline films of organic semiconductors. We showed how orientational effects supersede packing effects, investigating how out-of-plane quadrupolar moments can cause an electrostatic stabilization or destabilization of charge carriers, irrespective of the packing motif. Our study of amorphous materials revealed that long-range effects persist even in structurally disordered systems as either a finite-sized induced simulation artifact, a result of residual structural correlations, or both.

■ ASSOCIATED CONTENT

Supporting Information

This material is available free of charge via the Internet at <http://pubs.acs.org/>. The Supporting Information is available free of charge on the ACS Publications website at DOI: 10.1021/acs.jctc.6b00599.

Derivation of the thin film and bulk shape factors, electrostatic and induction expressions, lists of interaction kernels, and 2D-Ewald potentials. (PDF)
Input files for the VOTCA program (ZIP)

■ AUTHOR INFORMATION

Corresponding Authors

*E-mail: carl@poelking.org (C.P.).

*E-mail: denis.andrienko@mpip-mainz.mpg.de (D.A.).

Notes

The authors declare no competing financial interest.

■ ACKNOWLEDGMENTS

We are grateful for financial support from the BMBF project MEDOS (FKZ 03EK3503B) and MESOMERIE (FKZ 13N10723), as well as the NMP-20-2014: Widening materials models program (project MOSTOPHOS, grant 646259). We thank Tristan Berau for comments on the manuscript.

■ REFERENCES

- (1) May, V.; Kühn, O. *Charge and Energy Transfer Dynamics in Molecular Systems*, 3rd ed.; Wiley-VCH: Weinheim, 2011.
- (2) Miller, J. H., Jr.; Villagrán, M. Y. S.; Maric, S.; Briggs, J. M. *Phys. B* **2015**, *460*, 119–125.
- (3) Kaneko, M.; Okada, T. In *Molecular Catalysts for Energy Conversion*; Okada, D. T., Kaneko, P. D. M., Eds.; Springer Series in Materials Science 111; Springer: Berlin, 2009; pp 37–65.
- (4) Lin, P.; Yan, F. *Adv. Mater.* **2012**, *24*, 34–51.
- (5) Yost, S. R.; Van Voorhis, T. J. *Phys. Chem. C* **2013**, *117*, 5617–5625.

- (6) Ryno, S. M.; Risko, C.; Brédas, J.-L. *J. Am. Chem. Soc.* **2014**, *136*, 6421–6427.
- (7) Idé, J.; Méreau, R.; Ducasse, L.; Castet, F.; Bock, H.; Olivier, Y.; Cornil, J.; Beljonne, D.; D'Avino, G.; Roscioni, O. M.; Muccioli, L.; Zannoni, C. *J. Am. Chem. Soc.* **2014**, *136*, 2911–2920.
- (8) Kordt, P.; van der Holst, J. J. M.; Al Helwi, M.; Kowalsky, W.; May, F.; Badinski, A.; Lennartz, C.; Andrienko, D. *Adv. Funct. Mater.* **2015**, *25*, 1955–1971.
- (9) Yavuz, I.; Martin, B. N.; Park, J.; Houk, K. N. *J. Am. Chem. Soc.* **2015**, *137*, 2856–2866.
- (10) Rühle, V.; Lukyanov, A.; May, F.; Schrader, M.; Vehoff, T.; Kirkpatrick, J.; Baumeier, B.; Andrienko, D. *J. Chem. Theory Comput.* **2011**, *7*, 3335–3345.
- (11) Baumeier, B.; Stenzel, O.; Poelking, C.; Andrienko, D.; Schmidt, V. *Phys. Rev. B: Condens. Matter Mater. Phys.* **2012**, *86*, 184202.
- (12) Stenzel, O.; Hirsch, C.; Brereton, T.; Baumeier, B.; Andrienko, D.; Kroese, D.; Schmidt, V. *Multiscale Model. Simul.* **2014**, *12*, 1108–1134.
- (13) Kordt, P.; Stenzel, O.; Baumeier, B.; Schmidt, V.; Andrienko, D. *J. Chem. Theory Comput.* **2014**, *10*, 2508–2513.
- (14) Gemünden, P.; Poelking, C.; Kremer, K.; Andrienko, D.; Daoulas, K. C. *Macromolecules* **2013**, *46*, 5762–5774.
- (15) Gemünden, P.; Poelking, C.; Kremer, K.; Daoulas, K.; Andrienko, D. *Macromol. Rapid Commun.* **2015**, *36*, 1047–1053.
- (16) Poelking, C.; Tietze, M.; Elschner, C.; Olthof, S.; Hertel, D.; Baumeier, B.; Würthner, F.; Meerholz, K.; Leo, K.; Andrienko, D. *Nat. Mater.* **2014**, *14*, 434–439.
- (17) Poelking, C.; Andrienko, D. *J. Am. Chem. Soc.* **2015**, *137*, 6320–6326.
- (18) de Leeuw, S. W.; Perram, J. W.; Smith, E. R. *Proc. R. Soc. London, Ser. A* **1980**, *373*, 27–56.
- (19) de Leeuw, S. W.; Perram, J. W.; Smith, E. R. *Proc. R. Soc. London, Ser. A* **1980**, *373*, 57–66.
- (20) Smith, E. R. *Proc. R. Soc. London, Ser. A* **1981**, *375*, 475–505.
- (21) Fitzner, R.; Mena-Osteritz, E.; Mishra, A.; Schulz, G.; Reinold, E.; Weil, M.; Körner, C.; Ziehlke, H.; Elschner, C.; Leo, K.; Riede, M.; Pfeiffer, M.; Urich, C.; Bäuerle, P. *J. Am. Chem. Soc.* **2012**, *134*, 11064–11067.
- (22) Banerjee, R.; Novák, J.; Frank, C.; Lorch, C.; Hinderhofer, A.; Gerlach, A.; Schreiber, F. *Phys. Rev. Lett.* **2013**, *110*, 185506.
- (23) Wynands, D.; Erber, M.; Rentenberger, R.; Levichkova, M.; Walzer, K.; Eichhorn, K.-J.; Stamm, M. *Org. Electron.* **2012**, *13*, 885–893.
- (24) Schwarze, M.; Tress, W.; Beyer, B.; Gao, F.; Scholz, R.; Poelking, C.; Ortstein, K.; Günther, A. A.; Kasemann, D.; Andrienko, D.; Leo, K. *Science* **2016**, *352*, 1446–1449.
- (25) Ewald, P. P. *Ann. Phys. (Berlin, Ger.)* **1921**, *369*, 253–287.
- (26) Giese, T. J.; Panteva, M. T.; Chen, H.; York, D. M. *J. Chem. Theory Comput.* **2015**, *11*, 436–450.
- (27) Ren, P.; Ponder, J. W. *J. Phys. Chem. B* **2003**, *107*, 5933–5947.
- (28) Stone, A. J. *J. Chem. Theory Comput.* **2005**, *1*, 1128–1132.
- (29) D'Avino, G.; Muccioli, L.; Zannoni, C.; Beljonne, D.; Soos, Z. G. *J. Chem. Theory Comput.* **2014**, *10*, 4959–4971.
- (30) Thole, B. *Chem. Phys.* **1981**, *59*, 341–350.
- (31) Bereau, T.; Andrienko, D.; von Lilienfeld, O. A. *J. Chem. Theory Comput.* **2015**, *11*, 3225–3233.
- (32) Stone, A. J. *The Theory of Intermolecular Forces*; Clarendon Press: Oxford, 1997.
- (33) Misquitta, A. J.; Stone, A. J. *J. Chem. Phys.* **2006**, *124*, 024111.
- (34) Hättig, C.; Heß, B. A. *Mol. Phys.* **1994**, *81*, 813–824.
- (35) van Duijnen, P. T.; Swart, M. J. *Phys. Chem. A* **1998**, *102*, 2399–2407.
- (36) Leslie, M. *Mol. Phys.* **2008**, *106*, 1567–1578.
- (37) Smith, W. *CCPS Newsletter* **1998**, *46*, 18–30.
- (38) Kirkwood, J. G. *J. Chem. Phys.* **1934**, *2*, 351.
- (39) Hu, Z. *J. Chem. Theory Comput.* **2014**, *10*, 5254–5264.
- (40) Pan, C.; Hu, Z. *J. Chem. Theory Comput.* **2014**, *10*, 534–542.
- (41) Crozier, P. S.; Rowley, R. L.; Spohr, E.; Henderson, D. *J. Chem. Phys.* **2000**, *112*, 9253.
- (42) De Leeuw, S. W.; Perram, J. W. *Mol. Phys.* **1979**, *37*, 1313–1322.
- (43) Bürckstümmer, H.; Tulyakova, E. V.; Deppisch, M.; Lenze, M. R.; Kronenberg, N. M.; Gsänger, M.; Stolte, M.; Meerholz, K.; Würthner, F. *Angew. Chem., Int. Ed.* **2011**, *50*, 11628–11632.
- (44) Sun, S.-S.; Dalton, L. R., Eds.; *Introduction to Organic Electronic and Optoelectronic Materials and Devices*; Optical Science and Engineering 133; CRC Press: Boca Raton, 2008.
- (45) Mori, T.; Kim, H.-G.; Mizutani, T.; Lee, D.-C. *Jpn. J. Appl. Phys.* **2001**, *40*, 5346–5349.
- (46) Lukyanov, A.; Lennartz, C.; Andrienko, D. *Phys. Status Solidi A* **2009**, *206*, 2737–2742.
- (47) May, F.; Baumeier, B.; Lennartz, C.; Andrienko, D. *Phys. Rev. Lett.* **2012**, *109*, 136401.